
Bonifacio MA, Gentile PG, Ferreira AM, Cometa S, Giglio ED.
[Insight Into Halloysite Nanotubes-Loaded Gellan Gum Hydrogels For Soft
Tissue Engineering Applications.](#)
Carbohydrate Polymers (2017)
DOI: <http://dx.doi.org/10.1016/j.carbpol.2017.01.064>

Copyright:

© 2017. This manuscript version is made available under the [CC-BY-NC-ND 4.0 license](#)

DOI link to article:

<http://dx.doi.org/10.1016/j.carbpol.2017.01.064>

Date deposited:

25/01/2017

Embargo release date:

20 January 2018



This work is licensed under a
[Creative Commons Attribution-NonCommercial-NoDerivatives 4.0 International licence](#)

1 **Insight Into Halloysite Nanotubes-Loaded Gellan Gum Hydrogels For Soft**
2 **Tissue Engineering Applications**

3 *Maria A. Bonifacio,^{1†} Piergiorgio Gentile,^{2†} Ana M. Ferreira,² Stefania Cometa,³ Elvira De*
4 *Giglio ^{1*}*

5
6
7 ^{1*}Dept. of Chemistry, University of Bari Aldo Moro, Via E. Orabona 4, Bari, 70126, Italy.

8 maria.bonifacio@uniba.it;

9 ² School of Mechanical and Systems Engineering, Newcastle University, Stephenson Building,

10 Claremont Road, Newcastle upon Tyne, NE1 7RU, UK.

11 piergiorgio.gentile@newcastle.ac.uk; ana.ferreira-duarte@newcastle.ac.uk

12 ³Jaber Innovation s.r.l., via Calcutta 8, Rome, 00144, Italy.

13 stefania.cometa@virgilio.it

14 *[†] These authors equally contributed to the work.*

15

16 * Corresponding author. Tel/Fax: +39 080 5442021.

17 E-mail address: elvira.degiglio@uniba.it (E. De Giglio)

18

19 **Abstract**

20 A tri-component hydrogel, based on gellan gum (GG), glycerol (Gly) and halloysite nanotubes
21 (HNT), is proposed in this work for soft tissue engineering applications. The FDA-approved GG
22 polysaccharide has been recently exploited as biomaterial because its biomimetic features. Gly is
23 added as molecular spacer to improve hydrogel viscosity and mechanical properties. HNT
24 incorporation within the hydrogel offers the versatility to improve the GG-Gly biocompatibility
25 with potential incorporation of target biomolecules. In this work, hydrogels with different
26 composition ratios are physically crosslinked for tuning physico-mechanical properties. An accurate
27 physico-chemical characterization is reported. HNT addition leads to a water uptake decrease of 30-
28 35% and tuneable mechanical properties with a compressive Young's modulus ranging between 20
29 and 75kPa. Finally, *in vitro* study with human fibroblasts on GG-Gly hydrogels loaded with 25%
30 HNT offered the higher metabolic activities and cell survival up to 7 days of incubation.

31

32 **Keywords:** Gellan gum, Halloysite nanotubes (HNT), Hydrogel, Human fibroblasts, Tissue
33 engineering.

34

35 **Chemical compounds studied in this article**

36 Gellan gum (PubChem SID: 135330201); Halloysite nanotubes (PubChem CID: 121233131);

37 Glycerol (PubChem CID: 753); Calcium Chloride (PubChem CID: 5284359).

38 **1. Introduction**

39 In the last years, the role of biomaterials in tissue engineering has gone beyond the classic view of
40 passive support for cell growth: the knowledge of the wide array of cell-matrix interactions has led
41 to a more conscious selection of biomaterials that mimic the complex spatio-temporal cues of
42 extracellular matrix (Chen & Liu, 2016). Hydrogels represent an interesting class of materials, with
43 high water content, tunable properties and ease to be processed under physiological conditions
44 (Annabi et al., 2014; De Giglio et al., 2011). In this scenario, biopolymer-based hydrogels stand out
45 for biocompatible features, given by the remarkable similarity with extracellular matrix (Van
46 Vlierberghe et al., 2011). Polysaccharides (e.g. gellan gum, alginate and chitosan) have the further
47 advantage of releasing non-toxic monomers during degradation and, for this reason, are the most
48 investigated biopolymers for biomedical applications (Pasqui et al., 2012). Gellan gum is an
49 exopolysaccharide secreted by bacteria belonging to the *Sphingomonas* genus. Firstly isolated in
50 1979, gellan gum is currently manufactured *in vitro* by a straightforward fermentation process,
51 avoiding batch-to-batch availability often associated to biopolymers (Prajapati et al., 2013). It
52 consists of a linear chain of repeated tetrasaccharide units (L-rhamnose, D-glucose and D-
53 glucuronic acid), commercially available under different trade names (e.g. Phytigel™, Gelrite®,
54 Kelcogel®). In presence of cations, gellan gum undergoes a temperature-dependent gelation,
55 forming stable hydrogels (Smith et al., 2007). After FDA approval as a food additive, this
56 polysaccharide is widely exploited in food industry as thickening agent or emulsion stabilizer
57 (Giavasis et al., 2000). Moreover, the potential of gellan gum is being studied in order to obtain new
58 pharmaceutical formulations for oral, nasal and ophthalmic drug delivery (Osmałek et al., 2014;
59 Wang et al., 2008).

60 Furthermore, thanks to its versatility, gellan gum is attracting increasing interest in the biomedical
61 field and is being proposed for tissue engineering and regenerative medicine applications (Coutinho
62 et al., 2010; Santhanam et al., 2016). A pioneering study by Shoichet et al. exploited a gellan gum
63 matrix to support the adhesion and proliferation of neural stem cells, showing that the peptide-

64 modified gellan gum, together with the olfactory ensheathing glia, enhanced neural stem/progenitor
65 cell survival (Silva et al., 2012). Cell adhesion improvement was also the focus of other works,(da
66 Silva et al., 2014; Cerqueira et al., 2014) in which spongy-like gellan gum hydrogels were proposed
67 as off-the-shelf 3D structures able to mimic the physico-chemical properties of ECM. Further
68 application proposed recently by Mano and coworkers is the use of gellan gum as an injectable
69 biomaterial (in form of blend with type I collagen), for bone regeneration purposes (Oliveira et al.,
70 2016). The proposed biomaterial induced the differentiation of human adipose stem cells through a
71 mechanotransduction pathway, without any medium supplement. Furthermore, one of the most
72 promising strategies involving gellan gum provides the opportunity to develop composite materials
73 adding inorganic particles (e.g. bioglasses) to the polymeric matrix (Gorodzha et al., 2016). With
74 low filler loadings, the polymers mechanical features improve, as well as their bioactivity (Dawson
75 & Oreffo, 2013). Among the inorganic particles available, natural nanoclay minerals provide the
76 double advantage to be cost-effective and biocompatible (Lopes et al., 2014). Therefore, the aim of
77 this work was to propose an innovative composite biomaterial in order to: (1) obtain a composite
78 material with tunable physical and mechanical properties, and (2) evaluate its biological potential
79 for tissue engineering applications. Specifically, in this work, halloysite nanotubes (HNT) have
80 been proposed as inorganic fillers of gellan-based hydrogels. HNT are tubular aluminosilicate clays
81 with a unique combination of features which are finding applications in numerous fields (Du et al.,
82 2010). Beyond the broad availability, HNT are biocompatible and exhibit excellent mechanical
83 properties (Yuan et al., 2015; Bottino et al., 2015; Liu et al., 2012). Several studies have reported
84 the long-term stability and non-toxicity of HNT (White et al., 2012; Kamble et al., 2012). Being
85 naturally dispersed, they do not require exfoliation procedures essential to obtain nanolayers from
86 glass fibers or montmorillonite (Chalasanani et al., 2013). Moreover, HNT mesoporous lumen could
87 entrap bioactive molecules and subsequently release them, opening new frontiers in sustained drug
88 delivery (Du et al., 2010). On the other hand, the hydroxyl groups distribution on the HNT outer

89 and inner surfaces allow a finely adjustable reactivity, achieved by targeted functionalisation
90 (Zhang et al., 2016).

91 Some works on HNT composites with various polymers have been recently reported. As example,
92 Liu and coworkers prepared alginate-HNT composite sponges by freeze-drying method resulting in
93 increased scaffold stability and better fibroblast attachment (Liu et al., 2015). Similarly, chitosan
94 and HNT formed a nanocomposite with significant thermal and mechanical improvements
95 compared with the pure polymer (Liu et al., 2013). More recently, Fakhrullin et al. doped with HNT
96 a chitosan–agarose–gelatin matrix and proposed it as advanced biomaterial for tissue engineering
97 and sustained nanotube drug delivery (Naumenko et al., 2016). However, to the best of our
98 knowledge, a nanoclay-polymer composite based on HNT and gellan gum has never been
99 developed and investigated. This work aims at filling this gap, shedding light into the potential and
100 intriguing applications of this new GG-based composite in soft tissue engineering. In this study, the
101 preparation and characterization of hydrogels physically crosslinked with Ca^{2+} cations is reported.
102 The hydrogels have been prepared varying the concentrations of HNT and glycerol, used as
103 molecular spacer. Indeed, glycerol is commonly exploited as a biocompatible structural ameliorant
104 to improve the physical and mechanical properties (Zhao et al., 2014). The composite hydrogels
105 were characterized by morphological, physico-chemical and mechanical analyses. Ultimately,
106 human fibroblasts were seeded on the surface and encapsulated into the hydrogel in order to test the
107 potential applications as substrate or injectable biomaterial.

108

109 **2. Materials and methods**

110 **2.1 Materials**

111 Gellan gum (PhytigelTM, formula weight 1,000 kg/mol; low acylation degree), hereafter coded as
112 GG, halloysite nanoclay (HNT) and free flowing calcium chloride- Redi-driTM (CaCl_2) were all
113 supplied by Sigma-Aldrich (Italy). Glycerol (Gly) was provided by Baker Chemicals, Holland. The

114 ultrapure water employed throughout the experiments was obtained with a Milli-Q[®] Integral system
 115 equipped with a BioPak[®] ultrafiltration cartridge (Millipore, Merck).

116 **2.2 Sample preparation**

117 An aqueous solution of Gly (2 or 6% w/v) was heated at 90 °C and GG powder (2% w/v) added
 118 under vigorous stirring. To obtain the composite material, the dissolution step was followed by
 119 mixing with an aqueous suspension of HNT (final concentration 0, 0.2, 0.5 or 1% w/v), previously
 120 sonicated in cold water for 15 min. The codes and nominal compositions of the hydrogels are
 121 reported in Table 1.

122 *Table 1.* Nomenclature and nominal composition of the prepared hydrogels. All the % w/v are
 123 expressed in respect to the water.
 124

Sample Code	GG content [%w/v]	Gly content [%w/v]	CaCl ₂ content [%w/v]	HNT content [%w/v]
GG	2	--	0.025	--
GG-Gly(1:1)	2	2	0.025	--
GG-Gly(1:1)HNT10	2	2	0.025	0.2
GG-Gly(1:1)HNT25	2	2	0.025	0.5
GG-Gly(1:1)HNT50	2	2	0.025	1
GG-Gly(1:3)	2	6	0.025	--
GG-Gly(1:3)HNT10	2	6	0.025	0.2
GG-Gly(1:3)HNT25	2	6	0.025	0.5
GG-Gly(1:3)HNT50	2	6	0.025	1

125
 126 The obtained hydrogels were poured into 24-well plates (15.6 mm well diameter) and crosslinked
 127 with CaCl₂ (0.025% w/v) using the external gelation method described by Kaklamani et al. (2014).
 128 Briefly, two parallel porous microcellulose sheets, previously soaked in CaCl₂, were placed at the
 129 top and bottom of the polymer, providing the Ca²⁺ ions required to promote a reproducible and
 130 uniform gelation of the polymer. After 24 h, the gelled samples destined to chemical, thermal and
 131 morphological analyses were obtained by freezing at -20 °C for 24 h, followed by freeze-drying for
 132 48 h (Christ ALPHA 1-2/LD Plus, Martin Christ, Germany). Gelled samples employed for water
 133 uptake, mechanical and biological measurements were conditioned for 1 h in Phosphate-buffered

134 saline (PBS) solution prepared accordingly with Cold Spring Harbor Protocol. Samples used for the
135 water uptake evaluation were dried as above mentioned.

136 **2.3 Physico-chemical characterization**

137 *2.3.1 Scanning Electron Microscopy (SEM)*

138 Scanning electron microscope (Hitachi TM3030 Tabletop SEM) equipped with Energy Dispersive
139 Spectroscopy (EDS) was utilized to study the nanoclay dispersion into the composites, as well as its
140 dried morphology. The samples were cut into small cylinders (1.5 cm of diameter and 2 cm of
141 height), fixed on the aluminium stub using carbon tape. For pore size evaluation, 20 random pores
142 from at least three SEM images were analyzed by ImageJ software.

143 *2.3.2 Fourier Transform Infrared Spectroscopy in Attenuated Total Reflection mode (FT-IR/ATR)*

144 FT-IR/ATR analysis was performed on a Spectrum Two PE instrument using the Universal ATR
145 accessory (Single Reflection Diamond) (PerkinElmer Inc., Waltham, MA) at 4 cm⁻¹ resolution.
146 Dried samples were analyzed without any preliminary preparative step.

147 *2.3.3 X-ray Photoelectron Spectroscopy (XPS)*

148 XPS analysis was performed by a scanning microprobe PHI 5000 VersaProbe II (Physical
149 Electronics, Chanhassen, MN), equipped with a monochromatized AlK α X-ray radiation source.
150 The base pressure of the instrument to ensure vacuum in the analysis chamber was 10⁻⁹ mbar. The
151 X-ray take-off angle was 45° and the samples were analyzed in HP mode (scanned size about
152 1400x200 μ m). Survey scans (binding energy (BE) range 0–1200 eV, FAT mode, pass energy 117.4
153 eV) and high-resolution spectra (FAT mode, pass energy 29.35 eV) were recorded for each sample.
154 Data analysis of the latter was performed using the MultiPak software package (version 9.6.1.7,
155 which consists of a non-linear least-squares fitting program. The experimental points of the detailed
156 spectra were fitted using Gaussian–Lorentzian peaks having the same full width at half maximum
157 (FWHM). Charge referencing was performed by setting the lower binding energy C1s photo-peak
158 (i.e., C1s hydrocarbon peak) at 284.8 eV. Quantification (atomic percentage, At%) was made using
159 normalized peak area. The normalization of the peak area and comparison of data from different

160 elements was enabled by correction with empirically derived sensitivity factors according to
161 MultiPak library.

162 2.3.4 *Water uptake evaluation*

163 Dried polymeric samples were firstly weighed (m_{di}), successively placed in tea bags. The tea bags
164 containing the samples were sealed and immersed in PBS to determine the water uptake profile up
165 to 24 hours at 37°C. The tea bags containing samples were weighted prior (m_i^0) and after each time
166 point (m_i^t). Moreover, in order to guarantee that the amount of the measured water was only
167 ascribable to the samples swelling, the weight of empty wet tea bags after each time point (m_b^t) was
168 also considered. Therefore, the percentage of water uptake for each sample, along the time, was
169 calculated using the Equation 1 reported below:

$$170 \quad (WC\%)_i^t = \{[(m_i^t - m_b^t) - m_i^0] / m_{di}\} \times 100 \quad (1)$$

171 The test was performed in triplicate and results were reported as mean \pm standard deviation.

172 2.3.5 *Thermogravimetric Analysis (TGA)*

173 Thermogravimetric measurements were carried out by TGA TA-Instrument Q500, (Waters S.p.A.
174 Milan, Italy) in air atmosphere, following the thermic program: stabilisation at 30°C and isothermal
175 scan at 10°C min⁻¹ in the range 30-1000°C. Thermogravimetric (TG) and derivative
176 thermogravimetric (DTG) curves were evaluated.

177 2.3.6 *Mechanical tests: compression and stress-relaxation tests*

178 Mechanical tests of the gellan-based hydrogels were performed using a mechanical testing machine
179 (EZ-SX, Shimadzu, Japan). Test specimens were cylinder-shaped hydrogels with 1.6 cm diameter
180 with an average height of around 2 cm. Compression resistance of five samples for each
181 composition was evaluated at room temperature. The crosshead speed was set at 1 mm min⁻¹, and
182 the load was applied until the specimen was compressed to around 35% of its original height before
183 break. The compressive stress–strain curves were thus obtained from the average compressive
184 modulus and standard deviation were calculated for each composition. Precisely, compressive

185 modulus was calculated as the slope of the initial linear portion of the stress–strain curve (0-15%),
186 as reported by Mattioli-Belmonte et al. (2015). Moreover, as previously described (Gentile et al.,
187 2012; Ciardelli et al., 2010; Pfeiffer et al., 2008) the values of collapse strength and strain (σ^* and
188 e^* , respectively) were calculated. For evaluating stress relaxation properties the hydrogels disks
189 were deformed with impermeable plates to a compressive strain of 10% with a deformation rate of
190 50 mm min^{-1} , in order to approximate an instantaneous deformation. Within 10% compression, the
191 stresses versus strain relations of the gels were almost linear. Subsequently, the strain was held
192 constant for 1200 s, while the load was recorded as a function of time. The obtained data were
193 analyzed using the software MATLAB R2015a. By fitting a third order exponential decay
194 (Equation 2) to the relaxation curves the three relaxation times were acquired. The increase in stress
195 during straining was not included when fitting the relaxation curves.

$$196 \quad \sigma(t) = A1 * e^{-t/\tau_1} + A2 * e^{-t/\tau_2} + A3 * e^{-t/\tau_3} + y0 \quad (2)$$

197 Finally, in order to evaluate the viscosity of the gels, a first order exponential decay (Equation 3)
198 was fitted through the relaxation curves of every measurement.

$$199 \quad \sigma(t) = A * e^{-t/\tau} + y0 \quad (3)$$

200 In particular, the viscosity (η) is found by multiplying the relaxation time τ with the linear modulus
201 E_0 , obtained by fitting the initial linear part of the strain curve of the straining protocol and creating
202 a linear fit. The gels were tested as prepared and soaked in PBS during the stress-relaxation tests to
203 prevent dehydration (Zhao et al., 2010).

204 **2.4 Biological evaluation**

205 *2.4.1 Cell culture*

206 Neonatal Normal Human Dermal Fibroblasts (NHDF-Neo) were purchased from Lonza Biosciences
207 (Switzerland) and cultured as recommended by the seller. Briefly, fibroblasts were grown at 37°C ,
208 $5\% \text{ CO}_2$, in Dulbecco's Modified Eagle Medium (DMEM, Sigma) supplemented with 10% fetal

209 bovine serum (FBS), 2 mM L-glutamine and a 1% antibiotic mixture containing penicillin and
210 streptomycin (100 U mL⁻¹).

211 In order to perform biocompatibility assays, thin disks of gels (15 mm diameter and 25 of height)
212 were prepared in 24-well plates and UV-sterilized for 15 min on each side. A further incubation
213 with FBS was performed as previously described (Barbucci, 2009). A suspension of 2×10^4 cells in
214 DMEM was seeded dropwise on the top surface of gels and incubated at 37 °C, 5% CO₂ for 30 min.
215 Then, fresh DMEM was added up to 500 µL volume.

216 2.4.2 Cell encapsulation

217 To encapsulate cells, the GG solutions were kept under agitation and slowly cooled until a
218 temperature of 37 °C was reached. In a 24-multiwell plate, each sample solution was rapidly mixed
219 with an equal volume of a cell suspension in warm DMEM. The final cell density was 2×10^5 cells
220 mL⁻¹. When the gelation occurred, the encapsulated hydrogels were covered with additional DMEM
221 and incubated for 1, 3 and 7 days at 37°C.

222 2.4.3 Cytocompatibility studies

223 Cell viability was assessed with the live/dead staining (LIVE/DEAD® Cell Imaging Kit, Life
224 Technologies, Thermo Scientific, USA) at days 1, 3 and 7. According to the manufacturer's
225 protocol, samples were washed with phosphate buffered saline (PBS, Sigma-Aldrich, UK) and
226 stained with 150 µL solution of 4 µM Ethidium homodimer-1 and 2 µM calcein in PBS. After 35
227 minutes of incubation at room temperature, cells were imaged with a Leica DM/LB fluorescence
228 microscope using FITC and Rhodamine filters to detect calcein (ex/em 488 nm/515 nm) and
229 Ethidium homodimer-1 (ex/em 570 nm/602 nm), respectively. The Presto Blue assay was exploited
230 to test the metabolic activity of cells seeded on the gels after 1, 3, 5 and 7 days of culture. A LS-50B
231 Luminescence Spectrometer (Perkin Elmer, Waltham, MA) was used to measure the fluorescence
232 (560nm excitation and 590nm emission) after 5 h of incubation with a 10% aliquot of Presto Blue
233 (Thermo Scientific, USA). The obtained values were corrected subtracting the average fluorescence
234 of control wells. Histograms reported the percentage difference between samples and control

235 cultures. Results were expressed as mean \pm standard deviation. Samples for fluorescence
236 microscopy were fixed with paraformaldehyde 4% in PBS (15 min at room temperature),
237 permeabilized washing them in PBS/0.1% Tween 20 and blocked in goat's serum 3% in PBS (1 h at
238 room temperature). The samples were labelled with Phalloidin-FITC (Sigma, UK) for 20 min at RT
239 to stain F-actin fibers. After PBS washings, nuclei were counterstained with 4',6-diamidino-2-
240 phenylindole (VECTASHIELD[®] Antifade Mounting Medium with DAPI, VECTOR
241 LABORATORIES LTS, UK). Samples were observed with an A1 Confocal Laser Microscope
242 (Nikon, UK).

243 2.4.4 Statistical analysis

244 The significance of the results of PrestoBlue assay were assessed by a two-way repeated measures
245 ANOVA. The test was replicated three times for each sample. All data were expressed as mean \pm
246 SD. Statistical analysis was performed with GraphPad Prism 7.01 software. The statistical
247 differences between the tissue culture plastic control and the hydrogels were calculated using
248 Dunnett test. Statistical significance was declared at * $p < 0.05$, ** $p < 0.01$, *** $p < 0.001$ and
249 **** $p < 0.0001$, where the asterisks labelled the samples with a cell metabolic activity significantly
250 higher than the control.

251

252 3. Results and discussion

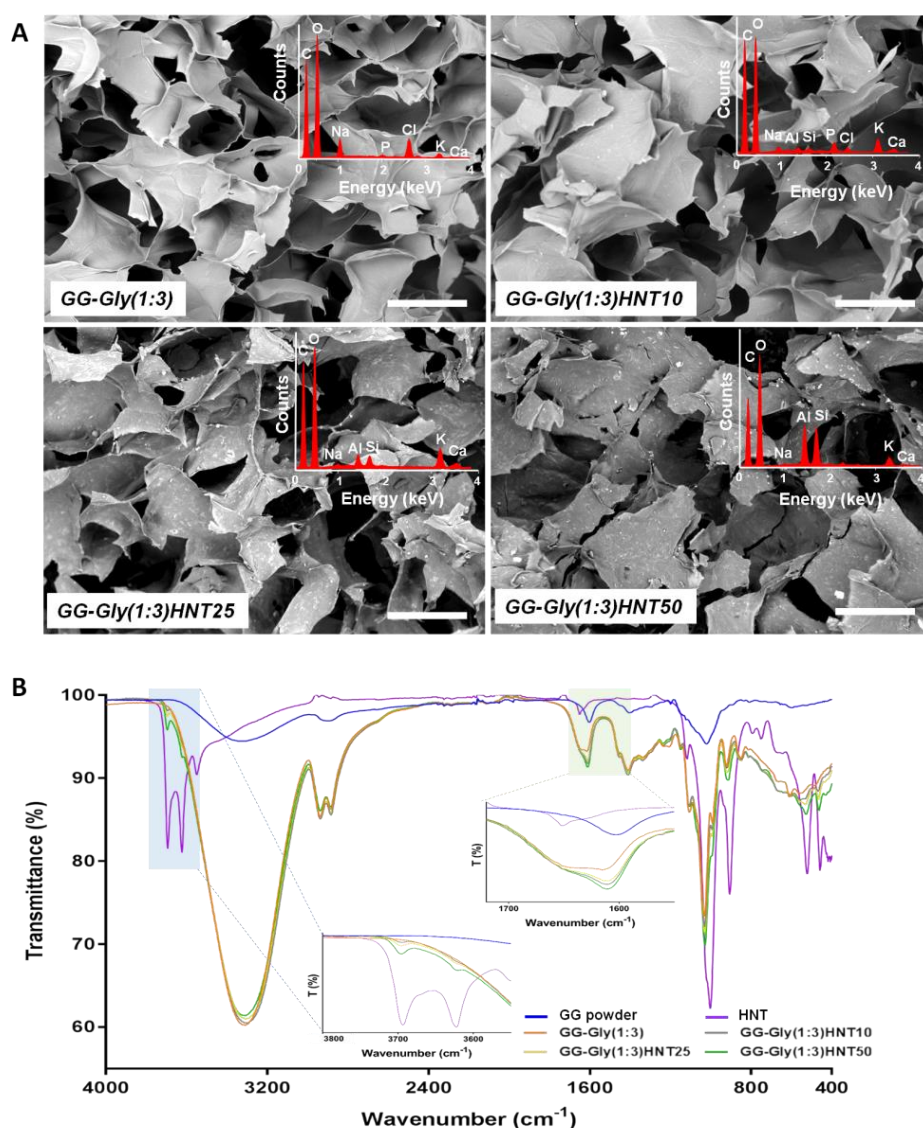
253 The physico-chemical characterization was carried out to evaluate the HNT influence and
254 interaction within the polymeric gels. However, some tests were performed on dried samples that,
255 during the PBS-conditioning and/or freeze-drying steps, lost not only water but also an appreciable
256 amount of glycerol. Therefore, the glycerol content detected in dried samples by FT-IR/ATR, XPS
257 and TGA techniques does not correspond to that present in the as prepared samples. Their
258 mechanical properties have been studied, as well as their citocompatibility. The biological behavior
259 of the hydrogels was evaluated for testing: (1) cell viability, metabolic activity and adhesion after
260 seeding fibroblasts on the gel top surface and (2) their ability to encapsulate cells for future

261 applications in 3D printing. Finally, for a better comprehension of the work, we decided to add
262 some figures/spectra of GG-Gly(1:1)HNTx samples in the *Supporting Information*, when they did
263 not show any significant differences respect with GG-Gly(1:3)HNTx samples.

264 **3.1. Physico-chemical characterization**

265 *3.1.1. Scanning electron microscopy (SEM)*

266 In Figure 1A and Figure S1, the SEM micrographs of the freeze-dried gel cross-sections relevant to
267 GG-Gly(1:3), GG-Gly(1:3)HNT10, Gly(1:3)HNT25 and GG-Gly(1:3)HNT50 were reported.



268
269 *Figure 1. SEM/EDS and FT-IR/ATR characterization. (A) SEM micrographs of GG-Gly(1:3)HNTx*
270 *samples, with x= 0, 10, 25 and 50. Scale bars: 500 μm. Insets: EDS spectra of the relevant samples.*
271 *(B) FT-IR/ATR spectra of HNT and GG powders, and GG-Gly(1:3)HNTx samples, with x=0, 10,*
272 *25 and 50.*

273

274 The SEM images provided insights into HNT dispersion within the polymeric network. No
275 significant changes in the sample microarchitecture could be highlighted after HNT addition. The
276 HNT presence was monitored through EDS analysis (see insets in Figure 1A and in Figure S1) by
277 the calculation of the amount of aluminium and silicon, the characteristic elements of the nanotubes.
278 Particularly, in the GG-Gly(1:3)HNT10 sample the relative aluminium abundance was 0.19 ± 0.04 ,
279 while the silicon amount was 0.17 ± 0.04 . For the GG-Gly(1:3)HNT25 sample, aluminium and
280 silicon were 0.56 ± 0.07 and 0.51 ± 0.07 . On the other hand, in the GG-Gly(1:3)HNT50 sample, the
281 aluminium and silicon elements were respectively 2.6 ± 0.2 and 2.5 ± 0.2 . However, at this
282 concentration, the nanoclays were more prone to aggregate and their dispersion in the polymeric
283 matrix was not as homogeneous as in GG-Gly(1:3)HNT10 and GG-Gly(1:3)HNT25 samples.
284 Moreover, since the combination of the selected polymer, molecular spacer and nanoclay was not
285 previously described, it was interesting to observe the texture achieved. The presence of glycerol
286 may have a role in enhancing the porosity of the system, as it could be observed comparing the
287 structure of all the other samples. Zhao et al. previously reported the impact of glycerol presence
288 during fabrication of different polymeric scaffolds, describing its role as porogen molecule at the
289 macroscopic level and as nanostructure ameliorant at the nanometric level. These effects were
290 ascribed to a decrease in flexibility of glycerol-interacted polymer chains, that led to the reduction
291 of polymeric conglomeration (Zhao et al., 2014). Finally, an evaluation of the systems porosity was
292 performed applying the same freeze-drying protocol for all the samples (see *par.* 2.2.1). GG-
293 Gly(1:3) showed pores of around $365 \pm 87 \mu\text{m}$, while HNT addition had no impact onto the
294 porosity, since the pore size for GG-Gly(1:3)HNT10, GG-Gly(1:3)HNT25 and GG-Gly(1:3)HNT50
295 were 290 ± 99 , 314 ± 84 and $285 \pm 82 \mu\text{m}$ respectively.

296 3.1.2. Fourier Transform Infrared Spectroscopy in Attenuated Total Reflection mode (FT-IR/ATR)

297 FT-IR/ATR spectra recorded on pure HNT and GG powder, and GG-Gly(1:3)HNT_x (with $x = 0$,
298 10, 25 and 50) samples were shown in Figure 1B. GG powder and the GG-based samples spectra

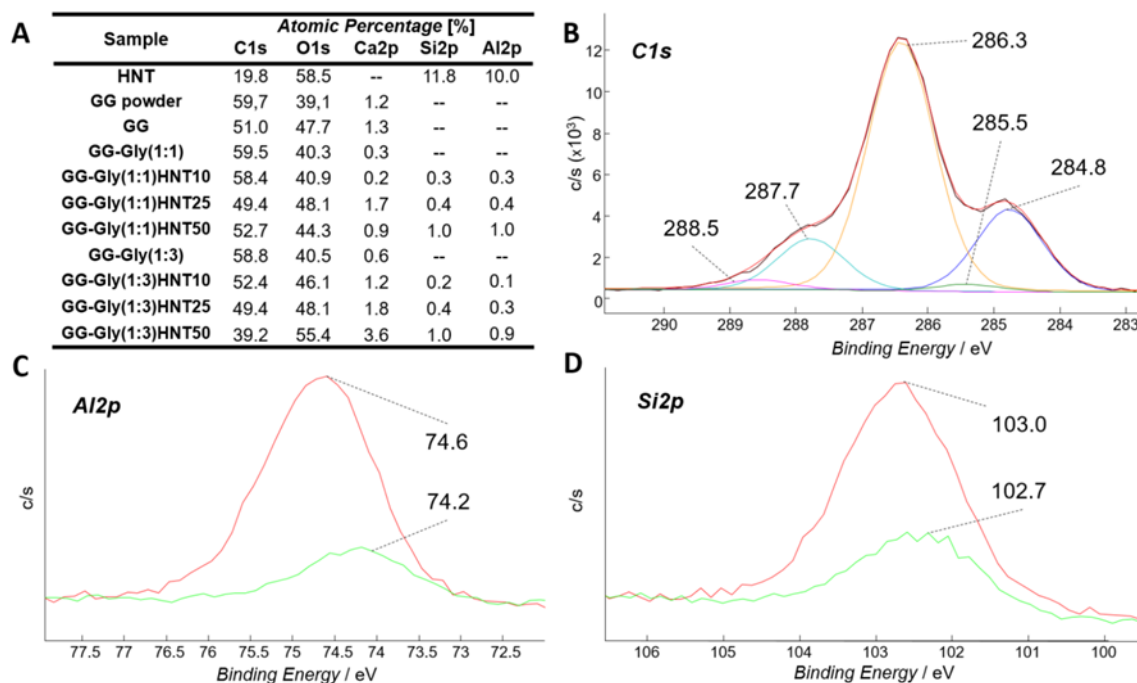
299 showed the band at 3311 cm^{-1} due to the presence of $-\text{OH}$ groups of glucopyranose ring. The band
300 at 2899 cm^{-1} was due to the stretching vibrations of $-\text{CH}_2$ groups, while those appearing at 1602 and
301 1403 cm^{-1} were due to asymmetric and symmetric stretching of $-\text{COO}^-$ groups. The absorption band
302 at 1145 cm^{-1} corresponded to antisymmetric C-O-C stretching of glycoside bonds, and the peak at
303 around 1010 cm^{-1} was attributable to C-OH stretching. In the case of the GG-based samples
304 crosslinked by Ca^{2+} , the presence of an additional band at 1656 cm^{-1} , visible as a shoulder on the
305 left of the main C=O stretching band falling at 1611 cm^{-1} and absent in pure GG powder, suggested
306 the interaction of $-\text{COO}^-$ groups with Ca^{2+} ions.

307 As far as HNT spectrum is concerned, the absorption peaks at 3693 , 3622 and 1652 cm^{-1} can be
308 associated to O-H stretching of inner hydroxyl groups and deformation of physisorbed water
309 molecules, as already reported (Chen, 2016). These features were also evident in the GG-
310 Gly(1:3)HNTx samples, in particular at higher HNT percentages (see insets in Figure 1B).
311 Furthermore, the samples based on GG-Gly(1:1) presented similar information observed on the GG-
312 Gly(1:3) series with only slight differences in the intensity of the chemical bands in the range 1500 -
313 1200 cm^{-1} and 1110 - 1000 cm^{-1} , due to the different glycerol content. Whereas, a more intense band
314 (at about 1610 cm^{-1}) in the GG-Gly(1:1) than in GG-Gly(1:3) series was related to the relative
315 higher GG weight in the composition of the former hydrogel (See Figure S2).

316 *3.1.3. X-ray Photoelectron Spectroscopy (XPS)*

317 XPS was employed to investigate the chemical composition of GG and HNT-containing hydrogels
318 after freeze-drying. Atomic percentages (At%) recorded on the different samples were reported in
319 Figure 2A. The analysis of GG powder showed the presence of the main elements of the polymer
320 (i.e., carbon and oxygen), in addition to minor contributions (i.e., potassium, calcium, magnesium
321 and sulfur), typical of gellan gum matrix as already reported by de Souza et al.(2016). For
322 simplicity these minor elements, falling in the range of $0.4 - 2.0\text{ At}\%$, were not reported, while
323 calcium signal, derived both from GG powder and the cross-linker, was considered. Beyond the
324 abundance of carbon and oxygen, it is worth to note the presence of silicon and aluminium in the

325 HNT-containing samples whose signal area ratios were about 1, as expected on the basis of the
 326 HNT stoichiometry.
 327 No XPS literature data are available on HNT-containing GG-based systems, therefore, an accurate
 328 curve fitting of C1s signals relevant to the investigated samples was carried out. In Figure 2B, high
 329 resolution C1s spectrum of GG-Gly(1:3)HNT25 was reported. No significant differences in C1s
 330 spectra relevant to the different HNT-based systems were detected. C1s spectra may be
 331 deconvoluted into five peak components associated with the following species: C-H (284.8 eV), C-
 332 COOR(H) (285.5 eV), C-OH (286.3 eV), O-C-O (287.7 eV) and COOR(H) (288.5 eV).



333 *Figure 2. XPS Analysis. (A) Atomic percentages (At%) recorded on pure HNT (casted from an*
 334 *aqueous solution on Au sheet), GG powder and on freeze-dried GG, GG-Gly(1:1)HNTx and GG-*
 335 *Gly(1:3)HNTx (with x=0, 10, 25, and 50) samples. (B) XPS curve fitting of high resolution C1s*
 336 *spectrum related to GG-Gly(1:3)HNT25 sample. (C) High-resolution XPS spectra of aluminium in*
 337 *pure HNT (red) and GG-Gly(1:3)HNT50 sample (green). (D) High-resolution XPS spectra of*
 338 *silicon in pure HNT (red) and GG-Gly(1:3)HNT50 sample (green).*
 339

340 The first peak, attributed to aliphatic carbon, did not belong only to gellan matrix but also to sample
 341 contamination as a result of adsorbed hydrocarbons monolayers. The last peak was slightly shifted
 342 from 288.8 (typical of carboxylic acid groups) to 288.5 eV, indicating a coordination between Ca²⁺
 343 and carboxylic acid groups, as already reported (Kang et al., 2015). Glycerol did not introduce

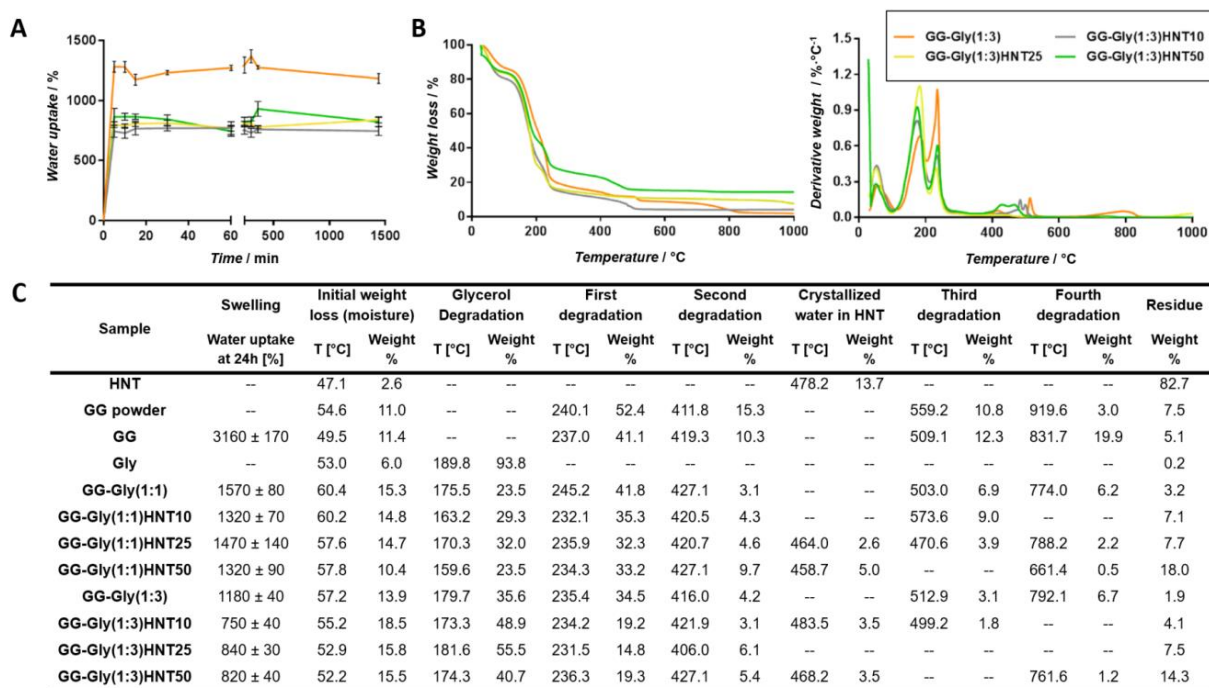
344 further peaks to C1s spectrum but its C-OH functionalities fell at 286.3 eV; anyway, its contribution
345 was markedly lower than that calculable from the starting amount due to the freeze-drying
346 procedure, as expected.

347 Figure 2C-D shows the high-resolution XPS spectra of aluminium and silicon in HNT (red line) and
348 GG-Gly(1:3)HNT50 sample (green line), where these contributions were more intense. It can be
349 observed a decrease (about 0.3-0.4 eV) in binding energy values of both silicon and aluminium
350 when HNT were loaded in the hydrogel matrix. This finding is related to the formation of hydrogen
351 bonds between the oxygen of Si-OH or Al-OH groups present in the nanoclays and hydrogen of the
352 organic network. A typical crystalline unit of HNT contains two types of hydroxyl groups, i.e., the
353 outer hydroxyl groups of the siloxane structure, where only a few of Si-OH groups are located in
354 HNT ends and surface defects, and the inner hydroxyl groups, due to the Al-OH groups situated in
355 the inner side. It can be hypothesized that the formation of hydrogen bonds between HNT and GG
356 and/or Gly involved not only most of the outer groups, but also the inner aluminols. An XPS
357 investigation of H-bond interactions in HNT-based polymer nanocomposites has been already
358 reported (Du et al., 2008), evidencing only interfacial interactions between the polymer matrix and
359 the Si-OH groups in HNT. In our case, glycerol intercalation into the HNT lumen could be invoked,
360 thus justifying the interaction between the inner Al-OH groups and glycerol hydroxyl groups (Liu et
361 al., 2011).

362 *3.1.4. Water uptake evaluation*

363 GG-based freeze-dried hydrogels were examined in terms of their swelling performances in PBS at
364 37 °C. Although the swelling measured on freeze-dried systems was not indicative of the real water
365 content of the as-prepared samples, this study allowed us to understand how the amount of HNT
366 can influence the water uptake properties of the proposed composites. The water uptake profile over
367 time of GG-Gly(1:3)HNTx specimens was reported in Figure 3A. The water uptake data at 24 hours
368 of all the examined samples were reported in Figure 3C. As shown in Figure 3A, the GG-Gly(1:3)-
369 based samples rapidly swelled upon contact with PBS, reaching a maximum just after five minutes

370 (i.e., around 800% and 1200% for samples with or without HNT respectively). This trend was
 371 observed also in the GG-Gly(1:1)HNTx series (Figure S3A). The presence of HNT, independently
 372 from their amount, was responsible in the GG-Gly(1:3) systems of an appreciable decrease of water
 373 uptake (reduction between 29 and 36%). Conversely, in the case of GG-Gly(1:1) samples, this
 374 reduction was lower (between 6 and 16%). These decreases in water uptake by the addition of HNT
 375 can be associated to the reduced hydrophilic polymer content in the composites (Huang et al.,
 376 2016). Indeed, the obtained water uptake in the 1:3 and 1:1 series meets the gellan gum content
 377 reported for freeze-dried samples.



378 *Figure 3.* Water uptake and Thermogravimetric Analysis. (A) Water uptake of GG-Gly(1:3)HNTx
 379 samples. (B) TGA and DTGA curves of GG-Gly(1:3)HNTx samples. (C) Water uptake data and
 380 thermal degradation steps of all the investigated samples.
 381

382 It is interesting to note that, after swelling, GG-Gly samples released high amounts of water upon
 383 contacting with blotting paper while GG-Gly-HNT samples showed a significantly high water
 384 retention, as shown in the photograph reported in Figure S3B. Since in both bare and HNT-loaded
 385 gels a comparable pore size was observed (see Figure 1A), the higher water retention capability of

386 HNT-loaded gels could be ascribed to a water intercalation into the HNT lumen. This feature makes
387 the proposed hydrogel an intriguing candidate as drug delivery system (Gupta & Shivakumar,
388 2010): the mesoporous HNT architecture could be exploited to intercalate different bioactive
389 molecules, delaying the release kinetics typical of highly porous polymers.

390 *3.1.5. Thermogravimetric Analysis (TGA)*

391 The overlay of TG (on the left) and DTG (on the right) signals, recorded on GG-Gly(1:3)HNTx
392 (with x=0,10,25 and 50) were reported in Figure 3B. The degradation steps, with the relevant
393 temperatures and weight loss percentages, were reported in Figure 3C for all examined samples
394 (i.e., the starting materials and the GG-Gly(1:1)HNTx and GG-Gly(1:3)HNTx series).

395 In particular, the GG powder thermogram indicated a weight loss of 11%, in the temperature range
396 from room to about 200°C, due to the water removal. The main degradation temperature was
397 centred at about 240°C. This first step of degradation promoted a weight loss of 52%, while the next
398 two steps promoted a weight loss of 15% at 412°C, relevant to loss of volatile components and
399 rupture of chain, and a weight loss of 11% at 559°C, relevant to fragmentation into monomers
400 (monosaccharide units). A fourth degradation step occurred at about 920°C (weight loss = 3%). The
401 remaining residue was of 7.5% of the initial weight of the sample. With regard to the GG based
402 sample, obtained by crosslinking with Ca²⁺ ions, the thermogram showed a weight loss of 11% due
403 to the water removal. The main degradation temperature was 237°C, with a weight loss of 41%. The
404 weight loss of crosslinked GG in the first stage decreased, indicating that the thermostability was
405 improved after the addition of the crosslinking agent. The next two steps promoted a weight loss of
406 10% at 419°C and 12% at 509°C, respectively. Finally, the last degradation step occurred at about
407 832°C, with a weight loss equal to 20%. The remaining residue was equal to 5% of the initial
408 weight of the sample.

409 The addition of glycerol in the samples, at different GG:Gly ratios (i.e., 1:1 and 1:3), was
410 responsible of the presence of an additional peak in the range 160-180°C, relevant to the
411 vaporization of Gly (that in pure glycerol occurred at 190°C). This thermal event caused a weight

412 loss of 24 and 36% in GG-Gly(1:1) and GG-Gly(1:3), respectively. Furthermore, as also reported in
413 XPS characterization, due to the freeze-drying procedure, the Gly contribution was markedly lower
414 than that calculable from the starting amounts.

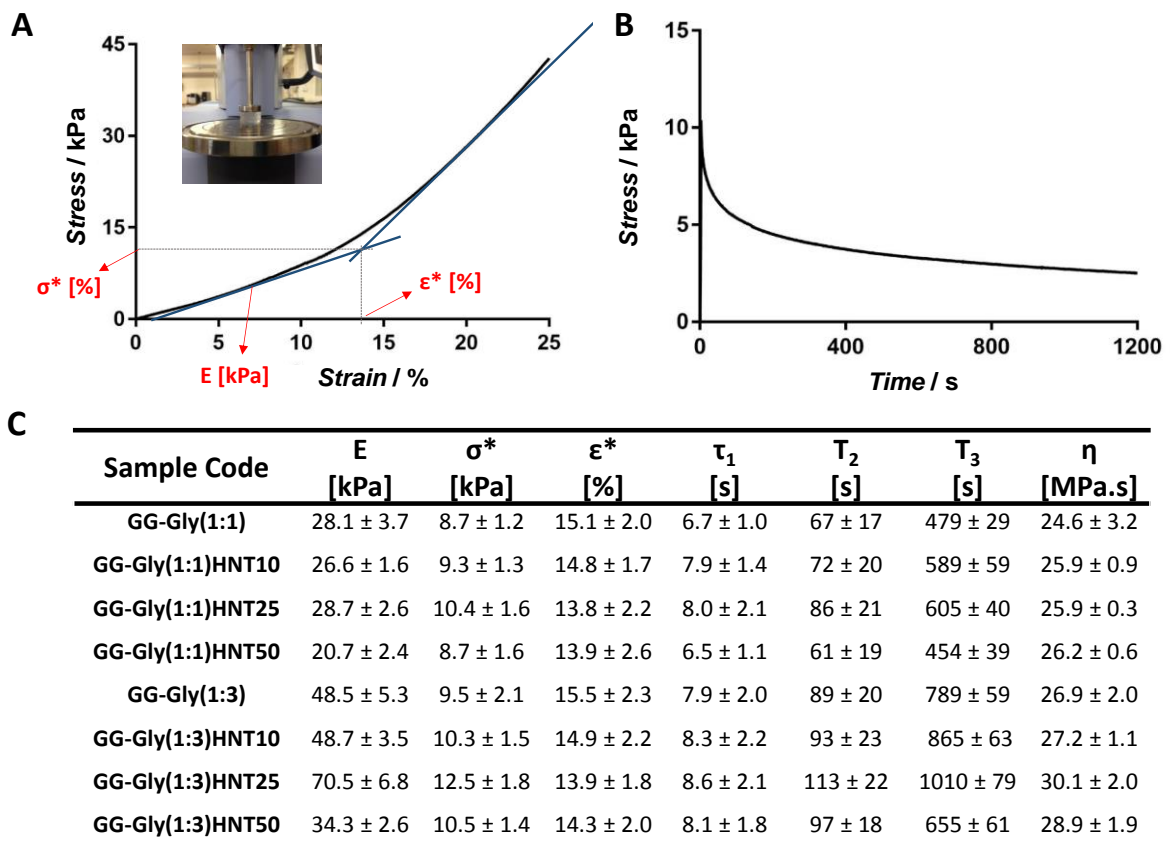
415 The HNT thermogram (plot not shown) exhibited a weight loss of 3.5% in the temperature range
416 from room to about 170°C, which was due to the loss of water and/or volatile compounds. The main
417 HNT mass loss of about 14%, centred at the temperature range of 478°C, was attributed to the
418 release of crystallization water (Jia et al., 2009). The residue at 1000°C in air was equal to 83%.
419 The HNT-containing samples revealed a residue at 1000°C in good agreement with their HNT feed
420 ratio (see the TG on the left of Figure 3B). Furthermore, in HNT-containing samples the glycerol
421 amount was markedly higher than in those without HNT. This finding substantiated the hypothesis
422 of hydrogen bonds formation between HNT hydroxyl groups and glycerol, observed by XPS
423 analysis.

424 3.1.6. Mechanical tests

425 The mechanical properties of the obtained hydrogels were tested using a mechanical testing
426 machine. Figure 4A showed the stress-strain curve obtained by the compression test at strain of 0-
427 25%. During the test, the hydrogels did not break but they underwent densifications. As described
428 previously by Gentile et al. (2012) the values of elastic modulus (E), collapse strength and strain
429 (σ^* and ϵ^* respectively) were calculated from the curves and listed in Figure 4C. A significant
430 improvement of the compressive modulus was observed by adding HNT (up to 25%) into the
431 polymeric gel (70.5 ± 6.8 kPa for GG-Gly(1:3)HNT25 compared with 48.5 ± 5.3 kPa for GG-
432 Gly(1:3)). The obtained values are higher or within the range of mechanical properties described for
433 other hydrogels proposed for soft tissue regeneration (Nettles et al., 2004; Balakrishnan et al.,
434 2014).

435 This mechanical reinforcement effect can be attributed to an additional energy-dissipating
436 mechanism introduced by the nanotubes in the polymeric gels. Recent molecular dynamics studies
437 suggested that this additional dissipative mechanism is a result of the mobility of the nanofillers.

438 During the deformation process, the HNT may orient and align under compression stress, creating
 439 temporary cross-links between polymer chains, thereby creating a local region of enhanced strength
 440 (Shah et al., 2005). However, when the amount of the nanotubes content increased, as in the GG-
 441 Gly(1:3)HNT50, they became less mobile. Therefore, the ability of the HNT to dissipate energy is
 442 also reduced, resulting in almost no improvement in the toughness of the material (34.3 ± 2.6 kPa).
 443 Furthermore the systems with higher Gly content demonstrated to be stiffer than those prepared
 444 with GG-Gly(1:1) with a maximum increase of 2.5-fold for the system containing 25% HNT (70.5
 445 ± 6.8 kPa for GG-Gly(1:3) respect with 28.7 ± 2.6 kPa for for GG-Gly(1:1)).



446
 447 *Figure 4.* Mechanical characterization. (A) Stress-strain curve obtained by compression test. (B)
 448 stress-relaxation curve. (C) Elastic modulus (E), collapse strength (σ^*), collapse strain (ϵ^*),
 449 relaxation times (τ_1 , τ_2 and τ_3) and viscosity (η) calculated for the prepared hydrogels.
 450

451 This effect has been described also by Lugao et al. (2002) where glycerol, added to polyvinyl
 452 pyrrolidone hydrogels for wound healing applications, increased the elasticity of the gels as a result
 453 of the plasticising effect. Given the nature of the time dependent response of hydrogels, in addition

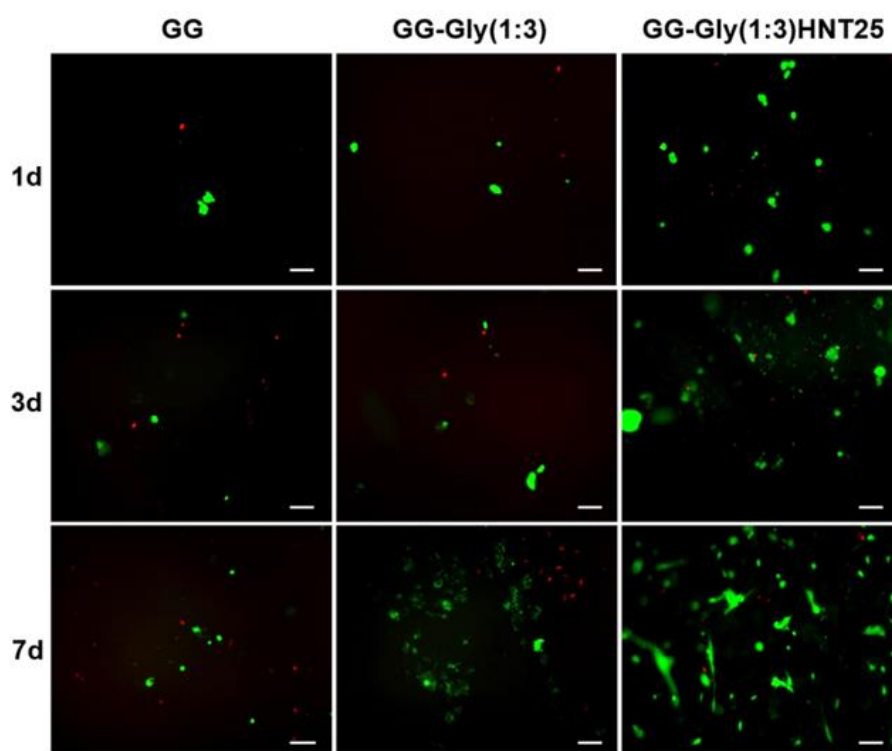
454 to simple tests at fixed rate, the samples were subjected to relaxation (load decrease at fixed strain)
455 experiments, where variation in response with time is of interest and the loading is fixed, in order to
456 evaluate the viscoelasticity behavior. These properties are fundamental, in combination with the
457 mechanical stiffness, to influence cell behavior as described recently by Chaudhuri et al. (2016)
458 where they studied how to regulate mesenchymal stem cell fate in hydrogels with tunable stress
459 relaxation. Figure 4B shows the typical stress relaxation curve obtained after 1200 s and the
460 relaxation times and viscosity values are listed in Figure 4C. Each material showed a two-stage
461 stress relaxation response: a fast decrease in stress for short times after the step strain, followed by a
462 slow relaxation covering a couple of decades of time. A generalized Maxwell model was used to
463 investigate whether the behavior could be explained by linear viscoelasticity, providing a range of
464 relaxation times and associated amplitudes that can approximate the viscoelastic behavior of
465 biological materials.

466 In literature, the generalized Maxwell model developed consisted of three relaxation times ($\tau_1 = 1$ -
467 10 s, $\tau_2 = 10$ -100 s and $\tau_3 > 1000$ s) for modelling soft biological tissues (Wagenseil et al., 2003).
468 In our work, relaxation times ranging from $\tau_1 = 6$ -9 s, $\tau_2 = 60$ -120 s and $\tau_3 = 600$ -1100 s were
469 comparable with the literature. Finally, it was observed that the addition of HNT did not influence
470 significantly the viscosity of the composite hydrogels (26.9 ± 2.0 MPa.s for GG-Gly(1:3) and 30.1
471 ± 2.0 MPa.s for GG-Gly(1:3)HNT25). However, the gels with higher content of glycerol revealed to
472 be more viscous comparing each system with the same content of HNT (25.9 ± 0.3 MPa.s for GG-
473 Gly(1:1)HNT25), due to the intrinsic glycerol capability to increase the viscosity of aqueous
474 solutions. Indeed, the addition of glycerol to synthetic and natural polymers enhanced hydrogels
475 viscosity, as already reported in literature (Fernandez-Diaz et al., 2001; Payen, 2007).

476 **3.2. Biological tests**

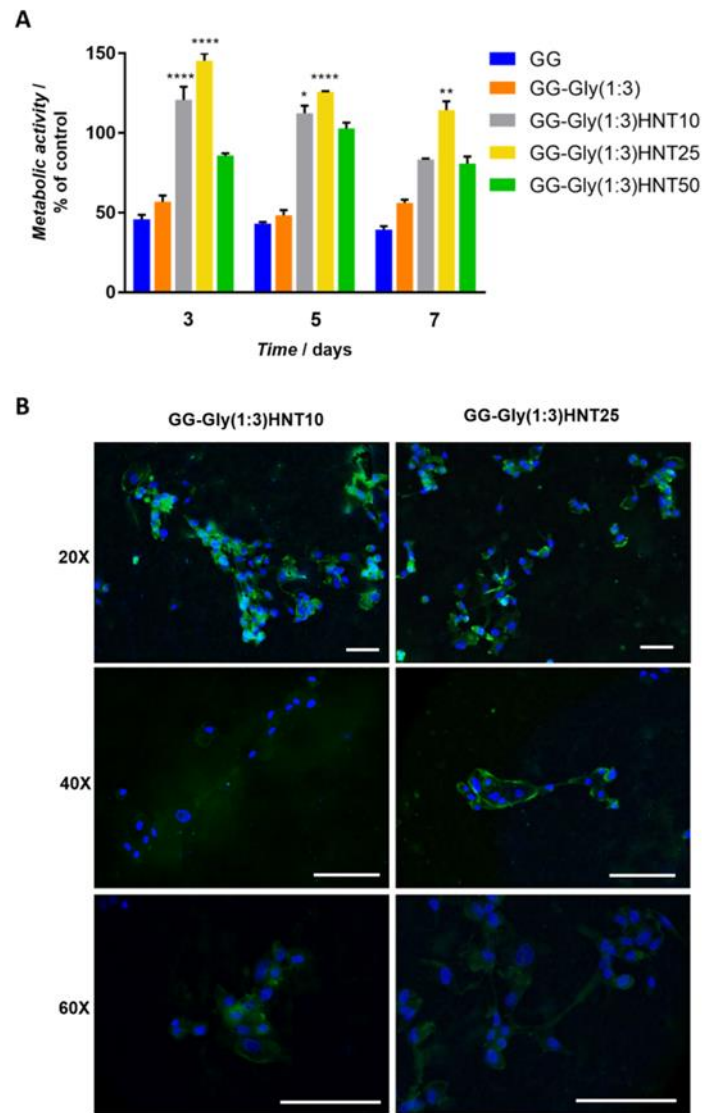
477 *3.2.1. Biocompatibility of the HNT-loaded hydrogels*

478 NHDF-Neo were seeded onto the surface of GG, GG-Gly (1:1)HNTx and GG-Gly (1:3)HNTx
479 hydrogels in order to evaluate the cytocompatibility of these materials. Cell viability was evaluated
480 after 1, 3 and 7 days by live/dead assay, as shown in Figure 5 and S3.
481 The bare gellan gum matrix GG showed a low cell viability and poor ability to promote cell
482 attachment. As reported in literature (Shin et al., 2014), the lack of adhesive signals in gellan gum
483 material do not favour cellular adhesion.. However, the addition of glycerol improved cell survival
484 on all the GG-Gly hydrogels studied. Furthermore, , it was found that the HNT addition to GG-Gly
485 hydrogels enhanced the cell viability, thanks to their biocompatibility and the increase in surface
486 roughness (Figure 6B) (Zhou et al., 2010; Kommireddy et al., 2005; Hughes et al., 2015; Huang et
487 al., 2016).



488
489 *Figure 5.* Live/Dead assay of cells seeded on hydrogel surfaces. Representative fluorescent
490 micrographs of live (green) and dead (red) cells seeded on GG, GG-Gly(1:3) and GG-
491 Gly(1:3)HNT25 after 1, 3 and 7 days of culture. Scale bars 200 μ m.
492

493 As shown on the surface of GG-Gly(1:3)HNT25 sample, cell viability was maintained and cell
 494 growth was enhanced at each time point (up to 7 days), as observed by the Live/dead and metabolic
 495 activity assays. Therefore, cell behavior seemed to be led by the combination of mechanical
 496 properties and HNT content.



497 *Figure 6.* Metabolic activity and morphological study of cells seeded on hydrogel surfaces. (A)
 498 PrestoBlue assay of cells cultured on GG and GG-Gly(1:3)HNTx hydrogels for 3, 5 and 7 days. (B)
 499 Fluorescence microscopy images of cells seeded on GG-Gly(1:3)HNT10 and GG-Gly(1:3)HNT25
 500 after 3 days of culture. Scale bars: 100 μ m.
 501
 502

503 The metabolic activity of NHDF-Neo was evaluated using Presto Blue assay (Figure 6A and S4),
 504 normalized by control (cells seeded onto tissue culture plastic) at each incubation time-point. These

505 data confirmed the results observed by the live/dead assay, where glycerol presence led to an
506 increase in cellular metabolic activity when compared to the bare GG hydrogel ($p < 0.05$). Glycerol
507 plays essential roles in several intracellular metabolic pathways (i.e., it forms the backbone of fats
508 such as triglycerides, and/or takes part in glycolysis or glycogenesis processes) and has been
509 exploited as a low-cost and biocompatible monomer to design scaffolds for tissue engineering
510 (Barrett et al., 2009). NHDF-Neo metabolic activity revealed a significant increase at each time
511 point by incorporating HNT within the GG:Gly hydrogel in different ratios, as seen for GG-Gly
512 (1:3)HNTx and GG-Gly (1:1)HNTx in Figure 6A and S4.

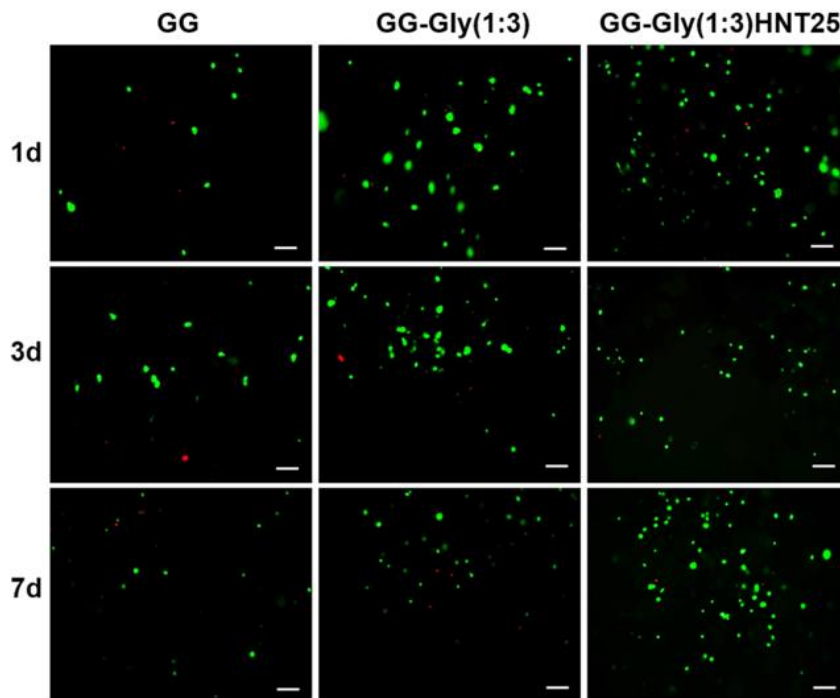
513 Interestingly, the hydrogel GG-Gly(1:3)HNT25 induced the highest fibroblasts metabolic activity
514 when compared to GG, GG-Gly, GG-Gly(1:3)HNT10 and GG-Gly(1:3)HNT50 ($p < 0.001$). Similar
515 results to those obtained for HNT-containing GG-Gly hydrogels were observed on halloysite-doped
516 dental scaffolds (Lvov et al., 2016; Vergaro et al., 2010). The HNT-loaded samples stimulated the
517 growth and promoted a faster fibroblasts spreading. However, a significant viability reduction was
518 observed on hydrogels with high HNT content (GG-Gly(1:3)HNT50), this can be explained by a
519 potential adverse effect of a concentrated halloysite, as described elsewhere (Lvov et al., 2016;
520 Vergaro et al., 2010).

521 Due to the best cell viability and metabolic activity performance, the fibroblast phenotype was
522 studied by fluorescence microscopy on GG-Gly(1:3)HNT25 and GG-Gly(1:3)HNT10 samples.
523 After 3 days of culture, NHDF-Neo exhibited their typically flattened and elongated morphology on
524 both hydrogels, spreading homogeneously along the sample surface and establishing many
525 intercellular contacts (Figure 6B).

526 3.2.2. Cells encapsulated

527 The NHDF-Neo were encapsulated within the GG-Gly hydrogels containing HNT and compared
528 with GG and GG:Gly control hydrogels. The cell viability of encapsulated cells within the different
529 hydrogels was assessed at 1, 3 and 7 days by Live/Dead assay (Figure 7 and Figure S6). The cells

530 encapsulated within the diverse systems showed a similar viability response to those observed when
531 seeded on the hydrogels surface (Figure 5).
532 A higher cell viability was detected within HNT-loaded samples in comparison with the bare GG
533 and GG-Gly hydrogels along the incubation period. It has been demonstrated that hydrogels
534 stiffness, microstructures and porosity, and material nature influence cellular functions such as cells
535 attachment and proliferation (Goponenko & Dzenis, 2016). As shown previously, the incorporation
536 of HNT enhanced the mechanical properties of the GG-Gly hydrogels and also improved the
537 biocompatibility of this material. Since cells were confined within the hydrogel matrix, no matter
538 how soft or stiff, the limited cell traction forces with substrate led to rounded cell morphology,
539 either within GG-Gly hydrogel and/or in presence of HNT.
540 This phenomenon has been widely reported in advanced 3D culture studies (Peyton & Putnam,
541 2005; Huebsch et al., 2010; Khetan et al., 2013; Murphy et al., 2014).



542 *Figure 7.* Live/Dead assay of hydrogel-encapsulated cells. Representative fluorescent micrographs
543 of live (green) and dead (red) cells encapsulated in GG, GG-Gly(1:3) and GG-Gly(1:3)HNT25 after
544 1, 3 and 7 days of culture. Scale bars 200 μ m.
545

546 **4. Conclusions**

547 Halloysite nanotubes have been integrated in gellan gum matrices to develop composite hydrogels
548 with tunable physical features, showing a good Human Dermal Fibroblasts biocompatibility when
549 cells were seeded on the top of the gels or encapsulated within the polymeric matrix. Fibroblasts
550 onto hydrogels with 25% HNT displayed the highest metabolic activity, which could be related to
551 the hydrogel mechanical and topographical features led by the HNT content. Gels presented suitable
552 mechanical properties to develop hydrogels scaffolds or injectable materials for different soft tissue
553 engineering applications (i.e. pancreas, liver, skin and chondral regeneration). Furthermore, the
554 hydrogels could be exploited to design *in vitro* cell culture systems and tissue models to study cell
555 behavior and interactions, mimicking the native microenvironments. In future, differentiation routes
556 of mesenchymal stem cells will be investigated, considering also the opportunity to functionalize
557 the HNT surface and mesoporous lumen with bioactive molecules able to elicit *in situ* advantageous
558 cell responses.

559

560 **Acknowledgments**

561 This work was supported by Università degli Studi di Bari Aldo Moro. Dr P. Gentile and Dr Ana
562 M. Ferreira are member of the UK EPSRC Centre for Innovative Manufacturing of Medical
563 Devices (MeDe Innovation, EPSRC grant EP/K029592/1). The authors would like to thank the
564 Bioimaging Unit at Newcastle University for supporting the confocal analysis. Dr Vincenzo
565 Schiavo is greatly acknowledged for his valuable support in TGA measurements. The authors
566 would also like to thank Mr Michael Foster for his helpful advice on SEM/EDX analysis, Mr
567 Stephen Moore for the kind support during the freeze-drying procedure and Mr Alex Boote for his
568 helpful contribution in mechanical test.

569

570

571

572 **References**

- 573 Annabi, N., Tamayol, A., Uquillas, J.A., Akbari, M., Bertassoni, L.E., Cha, C., Camci-Unal,
574 G., Dokmeci, M.R., Peppas, N.A., Khademhosseini, A. (2014). 25th anniversary article: rational
575 design and applications of hydrogels in regenerative medicine. *Advanced Materials*, 26, 85-124.
- 576 Balakrishnan, B., Joshi, N., Jayakrishnan, A., Banerjee, R. (2014). Self-crosslinked oxidized
577 alginate/gelatin hydrogel as injectable, adhesive biomimetic scaffolds for cartilage regeneration.
578 *Acta biomaterialia*, 10, 3650-63.
- 579 Barbucci, R. (2009). *Hydrogels: Biological properties and applications*, Milão: Springer,
580 (Chapter 8, p. 84).
- 581 Barrett, D.G., Yousaf, M.N. (2009). Design and applications of biodegradable polyester
582 tissue scaffolds based on endogenous monomers found in human metabolism. *Molecules*, 14, 4022-
583 50.
- 584 Bottino, M.C., Yassen, G.H., Platt, J.A., Labban, N., Windsor, L.J., Spolnik, K.J., Bressiani,
585 A.H.A. (2015). A novel three-dimensional scaffold for regenerative endodontics: materials and
586 biological characterizations. *Journal of tissue engineering and regenerative medicine*, 9, E116-E23.
- 587 Cerqueira, M.T., da Silva, L.P., Santos, T.C., Pirraco, R.r.P., Correlo, V.M., Reis, R.L.,
588 Marques, A.P. (2014). Gellan gum-hyaluronic acid spongy-like hydrogels and cells from adipose
589 tissue synergize promoting neoskin vascularization. *ACS applied materials & interfaces*, 6, 19668-
590 79.
- 591 Chalasani, R., Gupta, A., Vasudevan, S. (2013). Engineering new layered solids from
592 exfoliated inorganics: a periodically alternating hydroxalcite-montmorillonite layered hybrid.
593 *Scientific reports*, 3, 3498.
- 594 Chaudhuri, O., Gu, L., Klumpers, D., Darnell, M., Bencherif, S.A., Weaver, J.C., Huebsch,
595 N., Lee, H.P., Lippens, E., Duda, G.N. (2016). Hydrogels with tunable stress relaxation regulate
596 stem cell fate and activity. *Nature materials*, 15, 326-34.

597 Chen, F.M., Liu, X. (2016). Advancing biomaterials of human origin for tissue engineering.
598 *Progress in polymer science*, 53, 86-168.

599 Ciardelli, G., Gentile, P., Chiono, V., Mattioli-Belmonte, M., Vozzi, G., Barbani, N., Giusti,
600 P. (2010). Enzymatically crosslinked porous composite matrices for bone tissue regeneration.
601 *Journal of Biomedical Materials Research Part A*, 92, 137-51.

602 Coutinho, D.F., Sant, S.V., Shin, H., Oliveira, J.T., Gomes, M.E., Neves, N.M.,
603 Khademhosseini, A., Reis, R.L. (2010). Modified Gellan Gum hydrogels with tunable physical and
604 mechanical properties. *Biomaterials*, 31, 7494-502.

605 da Silva, L.P., Cerqueira, M.T., Sousa, R.A., Reis, R.L., Correlo, V.M., Marques, A.P.
606 (2014). Engineering cell-adhesive gellan gum spongy-like hydrogels for regenerative medicine
607 purposes. *Acta biomaterialia*, 10, 4787-97.

608 Dawson, J.I., Oreffo, R.O.C. (2013). Clay: new opportunities for tissue regeneration and
609 biomaterial design. *Advanced Materials*, 25, 4069-86.

610 De Giglio, E., Cometa, S., Ricci, M.A., Cafagna, D., Savino, A.M., Sabbatini, L., Orciani,
611 M., Ceci, E., Novello, L., Tantillo, G.M. (2011). Ciprofloxacin-modified electrosynthesized
612 hydrogel coatings to prevent titanium-implant-associated infections. *Acta biomaterialia*, 7, 882-91.

613 de Souza, F.S., de Mello Ferreira, I.L., da Silva Costa, M.A., de Lima, A.L.F., da Costa,
614 M.P.M., da Silva, G. M. (2016). Evaluation of different methods to prepare superabsorbent
615 hydrogels based on deacetylated gellan. *Carbohydrate polymers*, 148, 309-17.

616 Du, M., Guo, B., Lei, Y., Liu, M., Jia, D. (2008). Carboxylated butadiene–styrene
617 rubber/halloysite nanotube nanocomposites: interfacial interaction and performance. *Polymer*, 49,
618 4871-6.

619 Du, M., Guo, B., Jia, D. (2010). Newly emerging applications of halloysite nanotubes: a
620 review. *Polymer International*, 59, 574-82.

621 Fernandez-Díaz, M.D., Montero, P., Gomez-Guillen, M.C. (2001). Gel properties of
622 collagens from skins of cod (*Gadus morhua*) and hake (*Merluccius merluccius*) and their

623 modification by the coenhancers magnesium sulphate, glycerol and transglutaminase. *Food*
624 *Chemistry*, 74, 161-7.

625 Gentile, P., Mattioli-Belmonte, M., Chiono, V., Ferretti, C., Baino, F., Tonda-Turo, C.,
626 Vitale-Brovarone, C., Pashkuleva, I., Reis, R.L., Ciardelli, G. (2012). Bioactive glass/polymer
627 composite scaffolds mimicking bone tissue. *Journal of Biomedical Materials Research Part A*, 100,
628 2654-67.

629 Giavasis, I., Harvey, L.M., McNeil, B. (2000). Gellan gum. Critical reviews in
630 biotechnology. *Critical reviews in biotechnology*, 20, 177-211.

631 Goponenko, A.V., Dzenis, Y.A. (2016) Role of mechanical factors in applications of
632 stimuli-responsive polymer gels–Status and prospects. *Polymer*, 101, 415-449.

633 Gorodzha, S. Douglas, T.E.L., Samal, S.K., Detsch, R., Cholewa-Kowalska, K.,
634 Braeckmans, K., Boccaccini, A.R., Skirtach, A.G., Weinhardt, V., Baumbach, T. (2016).
635 High-resolution synchrotron X-ray analysis of bioglass-enriched hydrogels. *Journal of Biomedical*
636 *Materials Research Part A*, 104, 1294-201.

637 Gupta, N.V., Shivakumar, H.G. (2010). Preparation and characterization of superporous
638 hydrogels as gastroretentive drug delivery system for rosiglitazone maleate. *Daru*, 18, 200-10.

639 Huang, B., Liu, M., Long, Z., Shen, Y., Zhou, C. (2016). Effects of halloysite nanotubes on
640 physical properties and cytocompatibility of alginate composite hydrogels. *Materials Science and*
641 *Engineering: C*, 70, 303-310.

642 Huebsch, N., Arany, P.R., Mao, A.S., Shvartsman, D., Ali, O.A., Bencherif, S.A., Rivera-
643 Feliciano, J., Mooney, D.J. (2010). Harnessing traction-mediated manipulation of the cell/matrix
644 interface to control stem-cell fate. *Nature materials*, 9, 518-26.

645 Hughes, A.D., Marsh, G., Waugh, R.E., Foster, D.G., King, M.R. (2015). Halloysite
646 nanotube coatings suppress leukocyte spreading. *Langmuir*, 31, 13553-60.

647 Jia, Z., Luo, Y., Guo, B., Yang, B., Du, M., Jia, D. (2009). Reinforcing and flame-retardant
648 effects of halloysite nanotubes on LLDPE. *Polymer-Plastics Technology and Engineering*, 48, 607-
649 13.

650 Kaklamani, G., Cheneler, D., Grover, L.M., Adams, M.J., Bowen, J. (2014). Mechanical
651 properties of alginate hydrogels manufactured using external gelation. *Journal of the mechanical
652 behavior of biomedical materials*, 36, 135-42.

653 Kamble, R., Ghag, M., Gaikwad, S., Panda, B.K. (2012). Halloysite Nanotubes and
654 Applications: A Review. *Journal of Advanced Scientific Research*, 3, 25-29.

655 Kang, D., Cai, Z., Jin, Q., Zhang, H. (2015). Bio-inspired composite films with integrative
656 properties based on the self-assembly of gellan gum–graphene oxide crosslinked nanohybrid
657 building blocks. *Carbon*, 91, 445-57.

658 Khetan, S., Guvendiren, M., Legant, W.R., Cohen, D.M., Chen, C.S., Burdick, J.A. (2013).
659 Degradation-mediated cellular traction directs stem cell fate in covalently crosslinked three-
660 dimensional hydrogels. *Nature materials*, 12, 458-65.

661 Kommireddy, D.S., Ichinose, I., Lvov, Y.M., Mills, D.K. (2005). Nanoparticle multilayers:
662 Surface modification for cell attachment and growth. *Journal of Biomedical Nanotechnology*, 1,
663 286-90.

664 Liu, H., Chaudhary, D., Yusa, S.I., Tadó, M.O. (2011). Glycerol/starch/Na⁺-montmorillonite
665 nanocomposites: a XRD, FTIR, DSC and 1 H NMR study. *Carbohydrate Polymers*, 83, 1591-7.

666 Liu, M., Zhang, Y., Wu, C., Xiong, S., Zhou, C. (2012). Chitosan/halloysite nanotubes
667 bionanocomposites: structure, mechanical properties and biocompatibility. *International journal of
668 biological macromolecules*, 51, 566-75.

669 Liu, M., Wu, C., Jiao, Y., Xiong, S., Zhou, C. (2013). Chitosan–halloysite nanotubes
670 nanocomposite scaffolds for tissue engineering. *Journal of Materials Chemistry B*, 1, 2078-89.

671 Liu, M., Dai, L., Shi, H., Xiong, S., Zhou, C. (2015). In vitro evaluation of
672 alginate/halloysite nanotube composite scaffolds for tissue engineering. *Materials Science and*
673 *Engineering: C*, 49, 700-12.

674 Lopes, A.C., Martins, P., Lanceros-Mendez, S. (2014). Aluminosilicate and aluminosilicate
675 based polymer composites: present status, applications and future trends. *Progress in Surface*
676 *Science* 89, 239-77.

677 Lugão, A.B., Rogero, S.O., Malmonge, S.M. (2002). Rheological behaviour of irradiated
678 wound dressing poly (vinyl pyrrolidone) hydrogels. *Radiation Physics and Chemistry*, 63, 543-6.

679 Lvov, Y., Wang, W., Zhang, L., Fakhrullin, R. (2016). Halloysite clay nanotubes for loading
680 and sustained release of functional compounds. *Advanced Materials*, 28, 1227-50.

681 **Mattioli-Belmonte, M., De Maria, C., Vitale-Brovarone, C., Baino, F., Dicarolo, M., Vozzi,**
682 **G. (2015). Pressure-activated microsyringe (PAM) fabrication of bioactive glass–poly**
683 **(lactic-co-glycolic acid) composite scaffolds for bone tissue regeneration. *Journal of tissue***
684 ***engineering and regenerative medicine*.**

685 Murphy, W.L., McDevitt, T.C., Engler, A.J. (2014). Materials as stem cell regulators.
686 *Nature materials*, 13, 547-57.

687 Naumenko, E.A., Guryanov, I.D., Yendluri, R., Lvov, Y.M., Fakhrullin, R.F. (2016). Clay
688 nanotube–biopolymer composite scaffolds for tissue engineering. *Nanoscale*, 8, 7257-71.

689 Nettles, D.L., Vail, T.P., Morgan, M.T., Grinstaff, M.W., Setton, L.A. (2004).
690 Photocrosslinkable hyaluronan as a scaffold for articular cartilage repair. *Annals of biomedical*
691 *engineering*, 32, 391-7.

692 Oliveira, M.B., Custódio, C.A., Gasperini, L., Reis, R.L., Mano, J.F. (2016). Autonomous
693 osteogenic differentiation of hASCs encapsulated in methacrylated gellan-gum hydrogels. *Acta*
694 *biomaterialia*, 41, 119-32.

695 Osmalek, T., Froelich, A., Tasarek, S. (2014). Application of gellan gum in pharmacy and
696 medicine. *International journal of pharmaceuticals*, 466, 328-40.

697 Pasqui, E., De Cagna, M., Barbucci, R. (2012). Polysaccharide-based hydrogels: the key role
698 of water in affecting mechanical properties. *Polymers*, 4, 1517-34.

699 Payen S. (2007). *Integration of Hydrogels and Plastics Into Microfabrication Processes*
700 *Towards a MEMS RF-Interrogated Biosensor*, University of California, Berkeley, ProQuest,
701 (Chapter 3, p. 37).

702 Peyton, S.R., Putnam, A.J. (2005). Extracellular matrix rigidity governs smooth muscle cell
703 motility in a biphasic fashion. *Journal of cellular physiology*, 204, 198-209.

704 Pfeiffer, E., Vickers, S.M., Frank, E., Grodzinsky, A.J., Spector, M. (2008). The effects of
705 glycosaminoglycan content on the compressive modulus of cartilage engineered in type II collagen
706 scaffolds. *Osteoarthritis and Cartilage*, 16, 1237-44.

707 Prajapati, V.D., Jani, G.K., Zala, B.S., Khutliwala, T.A. (2013). An insight into the
708 emerging exopolysaccharide gellan gum as a novel polymer. *Carbohydrate polymers*, 93, 670-8.

709 Santhanam, S., Liang, J., Struckhoff, J., Hamilton, P.D., Ravi, N. (2016). Biomimetic
710 hydrogel with tunable mechanical properties for vitreous substitutes. *Acta Biomaterialia*, 43, 327-
711 37.

712 Shah, D., Maiti, P., Jiang, D.D., Batt, C.A., Giannelis, E.P. (2005). Effect of nanoparticle
713 mobility on toughness of polymer nanocomposites. *Advanced Materials*, 17, 525-8.

714 Shin, H., Olsen, B.D., Khademhosseini, A. (2014). Gellan gum microgel-reinforced cell-
715 laden gelatin hydrogels. *Journal of Materials Chemistry B*, 2, 2508-16.

716 Silva, N.A., Cooke, M.J., Tam, R.Y., Sousa, N., Salgado, A.J., Reis, R.L., Shoichet, M.S.
717 (2012). The effects of peptide modified gellan gum and olfactory ensheathing glia cells on neural
718 stem/progenitor cell fate. *Biomaterials*, 33, 6345-54.

719 Smith, A.M., Shelton, R., Perrie, Y., Harris, J.J. (2007). An initial evaluation of gellan gum
720 as a material for tissue engineering applications. *Journal of biomaterials applications*, 22, 241-54.

721 Van Vlierberghe, S., Dubruel, P., Schacht, E. (2011). Biopolymer-based hydrogels as
722 scaffolds for tissue engineering applications: a review. *Biomacromolecules*, 12, 1387-408.

723 Vergaro, V., Abdullayev, E., Lvov, Y.M., Zeitoun, A., Cingolani, R., Rinaldi, R., Leporatti,
724 S. (2010). Cytocompatibility and uptake of halloysite clay nanotubes. *Biomacromolecules*, *11*, 820-
725 6.

726 Wagenseil, J.E., Wakatsuki, T., Okamoto, R.J., Zahalak, G.I., Elson, E.L. (2003). One-
727 dimensional viscoelastic behavior of fibroblast populated collagen matrices. *Journal of*
728 *biomechanical engineering*, *125*, 719-25.

729 Wang, C., Gong, Y., Lin, Y., Shen, J., Wang, D.A. (2008). A novel gellan gel-based
730 microcarrier for anchorage-dependent cell delivery. *Acta Biomaterialia*, *4*, 1226-34.

731 White, R.D., Bavykin, D.V., Walsh, F.C. (2012). The stability of halloysite nanotubes in
732 acidic and alkaline aqueous suspensions. *Nanotechnology*, *23*, 065705, 1-10.

733 Yuan, P., Tan, D., Annabi-Bergaya, F. (2015). Properties and applications of halloysite
734 nanotubes: recent research advances and future prospects. *Applied Clay Science*, *112*, 75-93.

735 Zhang, Y., Tang, A., Yang, H., Ouyang, J. (2016). Applications and interfaces of halloysite
736 nanocomposites. *Applied Clay Science*, *119*, 8-17.

737 Zhao, X., Huebsch, N., Mooney, D.J., Suo, Z. (2010). Stress-relaxation behavior in gels with
738 ionic and covalent crosslinks. *Journal of Applied Physics*, *107*, 063509-1.

739 Zhao, S., Shen, Z., Wang, J., Li, X., Zeng, Y., Wang, B., He, Y., Du, Y. (2014). Glycerol-
740 mediated nanostructure modification leading to improved transparency of porous polymeric
741 scaffolds for high performance 3D cell imaging. *Biomacromolecules*, *15*, 2521-31.

742 Zhou, W.Y., Guo, B., Liu, M., Liao, R., Rabie, A.B.M., Jia, D. (2010). Poly (vinyl
743 alcohol)/halloysite nanotubes bionanocomposite films: properties and in vitro osteoblasts and
744 fibroblasts response. *Journal of Biomedical Materials Research Part A*, *93*, 1574-87.

SUPPLEMENTARY MATERIAL

Insight Into Halloysite Nanotubes-Loaded Gellan Gum Hydrogels For Tissue Engineering Applications

Maria A. Bonifacio,^{1†} Piergiorgio Gentile,^{2†} Ana M. Ferreira,² Stefania Cometa,³ Elvira De Giglio^{1}*

¹Dept. of Chemistry, University of Bari Aldo Moro, Via E. Orabona 4, Bari, 70126, Italy.

maria.bonifacio@uniba.it;

² School of Mechanical and Systems Engineering, Newcastle University, Stephenson Building, Claremont Road, Newcastle upon Tyne, NE1 7RU, UK.

piergiorgio.gentile@newcastle.ac.uk; ana.ferreira-duarte@newcastle.ac.uk

³Jaber Innovation s.r.l., via Calcutta 8, Rome, 00144, Italy.

stefania.cometa@virgilio.it

† These authors equally contributed to the work.

* Corresponding author. Tel/Fax: +39 080 5442021.

E-mail address: elvira.degiglio@uniba.it (E. De Giglio)

Keywords: Gellan gum, Halloysite nanotubes (HNT), Hydrogel, Human fibroblasts, Tissue engineering.

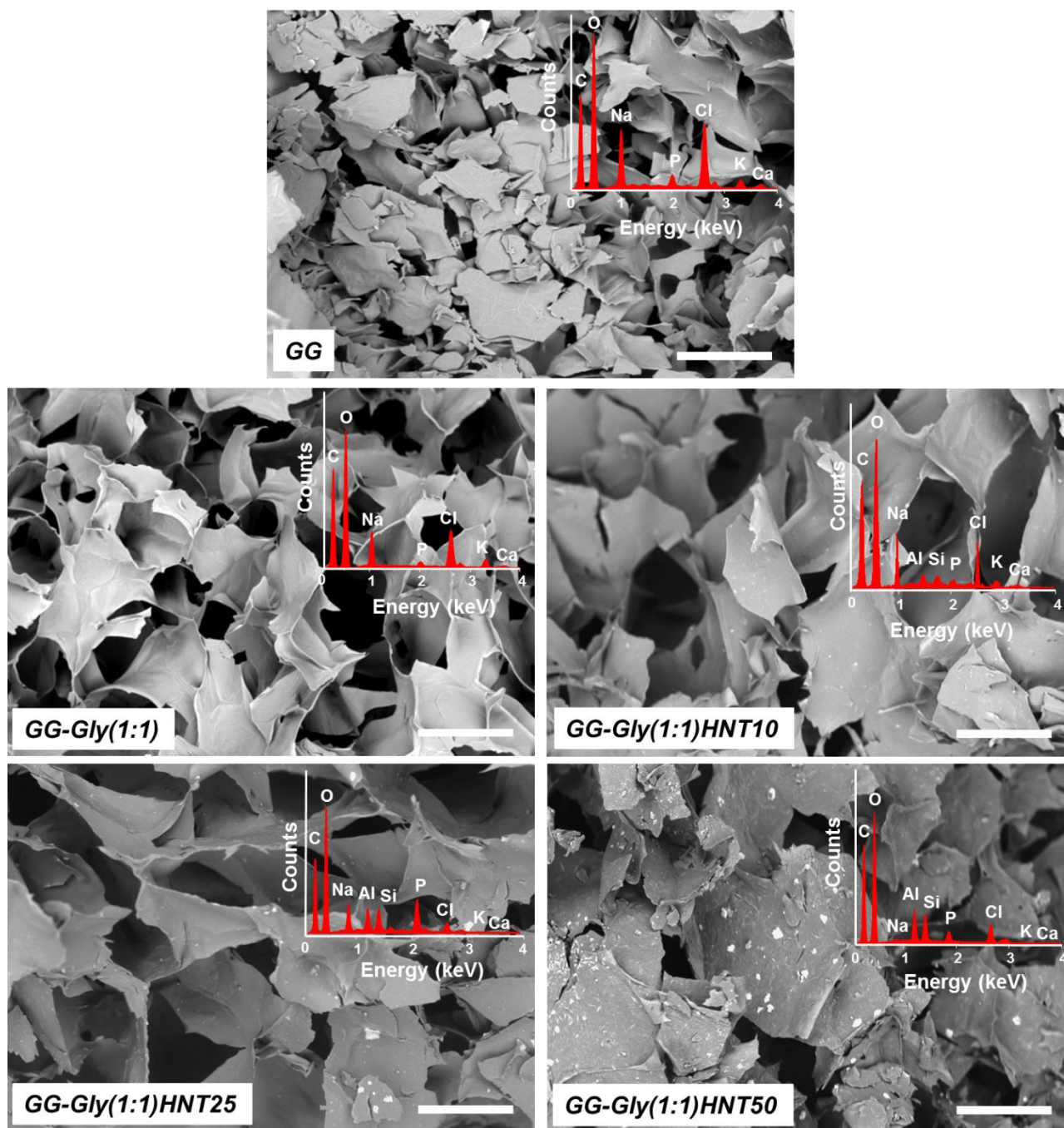


Figure S1. SEM/EDS characterization. SEM micrographs of GG and GG-Gly(1:1)HNT x samples, with $x=0, 10, 25$ and 50 . Scale bars: $500\ \mu\text{m}$. Pore size: $108 \pm 33\ \mu\text{m}$ for GG; $298 \pm 97\ \mu\text{m}$ for GG-Gly(1:1); $274 \pm 50\ \mu\text{m}$ for GG-Gly(1:1)HNT10, $313 \pm 56\ \mu\text{m}$ for GG-Gly(1:1)HNT25 and $267 \pm 70\ \mu\text{m}$ for GG-Gly(1:1)HNT50.

Insets: EDS spectra of the relevant samples. Relative Aluminum abundances in GG-Gly(1:1)HNT10, GG-Gly(1:1)HNT25 and GG-Gly(1:1)HNT50 samples are respectively: 0.26 ± 0.05 , 1.16 ± 0.13 and 2.8 ± 0.2 . Relative Silicon abundances in GG-Gly(1:1)HNT10, GG-Gly(1:1)HNT25 and GG-Gly(1:1)HNT50 samples are respectively: 0.23 ± 0.04 , 1.09 ± 0.12 and 2.6 ± 0.2 .

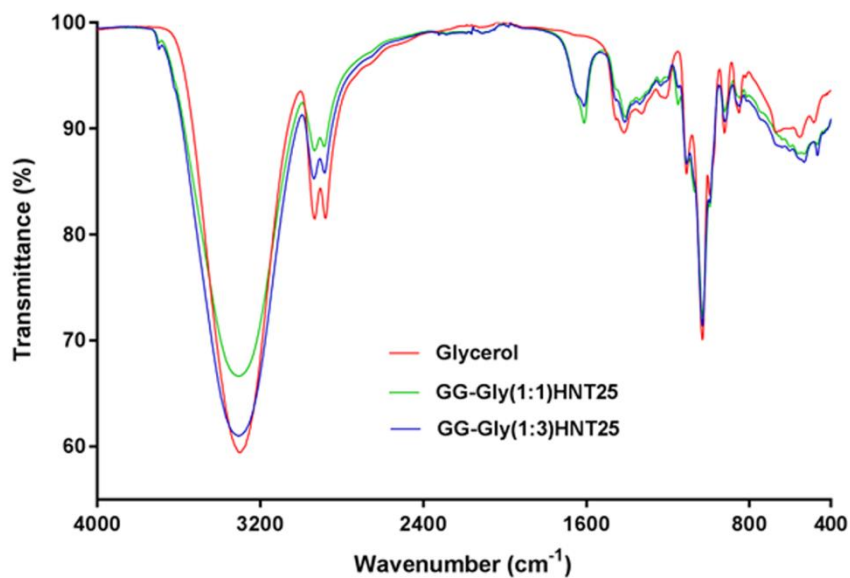


Figure S2. FT-IR/ATR characterization. Comparison between the spectra of pure glycerol, GG-Gly(1:1)HNT25 and GG-Gly(1:3)HNT25 samples.

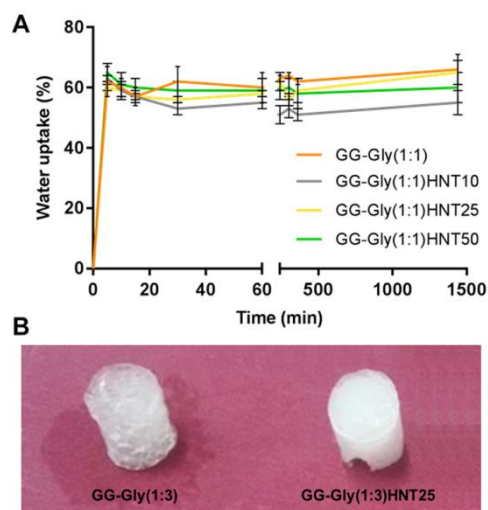


Figure S3. Water uptake and retention. (A) Water uptake of GG-Gly(1:1)HNTx samples. (B) Comparison of liquid retention between GG-Gly(1:3) (on the left) and GG-Gly(1:3)HNT25 (on the right) samples.

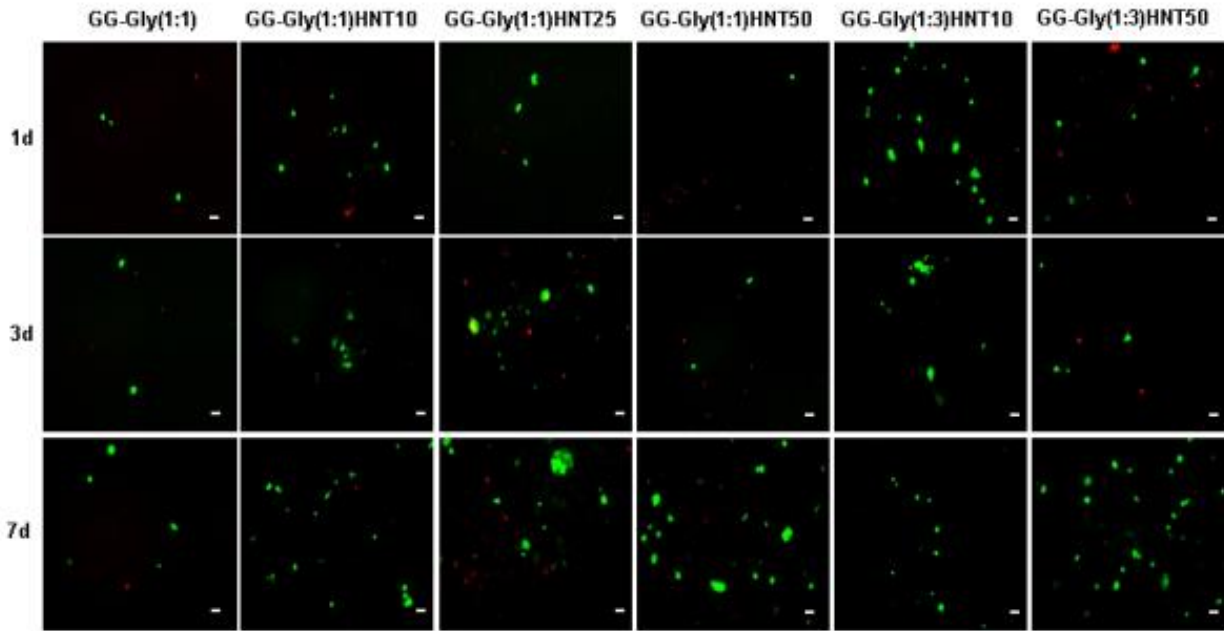


Figure S4. Live/Dead assay of cells seeded on hydrogel surfaces. Representative fluorescence micrographs of live (green) and dead (red) cells seeded on GG-Gly(1:1), GG-Gly(1:1)HNT10, Gly(1:1)HNT25, Gly(1:1)HNT50, Gly(1:3)HNT10 and Gly(1:3)HNT50 after 1, 3 and 7 days of culture. Scale bars 200µm.

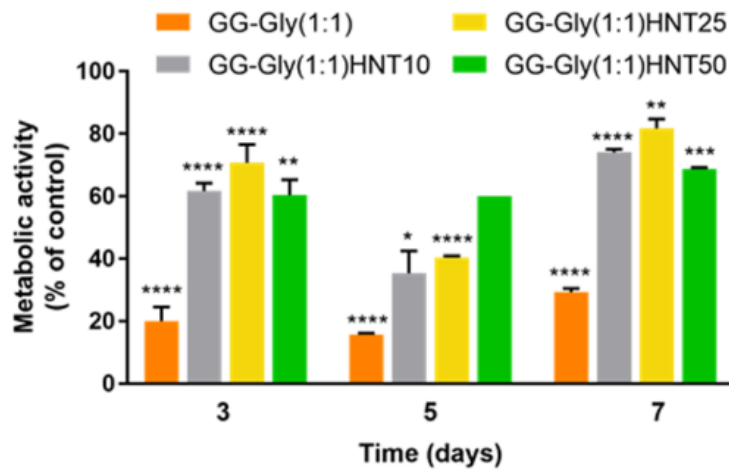


Figure S5. Metabolic activity of cells seeded on hydrogel surfaces. PrestoBlue assay of cells cultured on GG-Gly(1:1)HNTx hydrogels for 3,5 and 7 days.

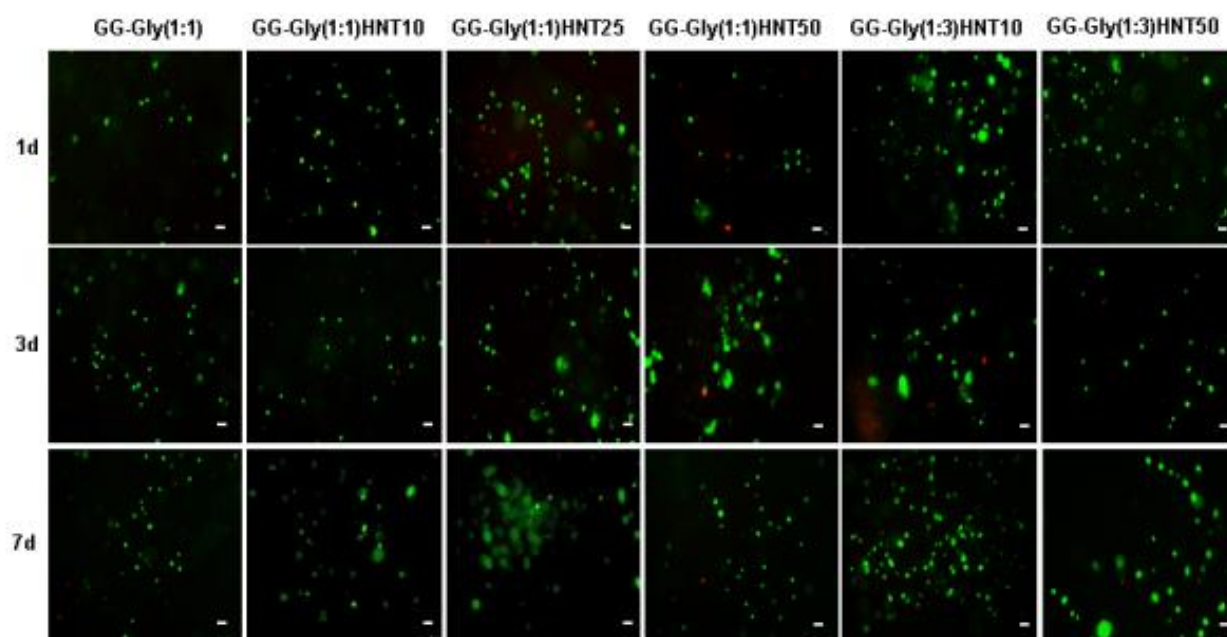


Figure S6. Live/Dead assay of hydrogel-encapsulated cells. Representative fluorescent micrographs of live (green) and dead (red) cells encapsulated in GG-Gly(1:1), GG-Gly(1:1)HNT10, Gly(1:1)HNT25, Gly(1:1)HNT50, Gly(1:3)HNT10 and Gly(1:3)HNT50 after 1, 3 and 7 days of culture. Scale bars 200 μ m.